PNAS
www.pnas.org

Supplementary Information for

The evolution of rock friction is more sensitive to slip than elapsed time, even at near-zero slip rates.

Pathikrit Bhattacharya, Allan M. Rubin, Terry E. Tullis, Nicholas M. Beeler and Keishi Okazaki

Pathikrit Bhattacharya.
E-mail: path_geoalum@alumni.princeton.edu

This PDF file includes:

Supplementary text
Figs. S1 to S19
References for SI reference citations

Supporting Information Text

1. Experimental apparatus and sample preparation

The friction experiments were performed on paired rings of Westerly granite using a gas-medium, high-pressure, rotary shear deformation apparatus at Brown University (Figure S2). The apparatus consists of a cylindrical pressure vessel, a pressure-generating system for confining pressure (Pc) and pore pressure (Pp), and axial and torsional loading systems (1–4). The torque (i.e., shear stress), the axial load, the axial shortening, and the rotation (i.e., shear displacement) are measured inside the pressure vessel nearby the sample rings (Figure S3). Therefore, frictional resistances from high pressure seals are not included for both stress and displacement measurements. The rotation is measured using a resolver with a digital 24-bit resolution per revolution pegging the resolution for the rotation of the sample at about 2×10^{-5} degree. This corresponds to a resolution of 9.2 nm on the recorded displacement with a circumferential sample length of 153.6 mm.

In this system, the axial load is controlled by a hydraulic servo-system. In addition, to minimize any elastic distortion being recorded as apparent slip during the velocity step, the torsional loading system is also controlled by a combination of hydraulic servo-system and an electro-hydraulic stepping motor with a feedback of the signal from the internal resolver for the shear displacement. This servo control system artificially increases the apparatus stiffness k more than an order of magnitude, depending on the experimental sample type, from about 0.0019 μm^{-1} (5, 6) to about 0.065 μm^{-1} (expressed as friction, i.e., shear stress/normal stress) at a normal stress of 25 MPa (Figure S4). This value implies that the elastic distortion by a change of shear stress $\Delta\tau$ of 2.5 MPa (equivalent to 0.1 change in friction at 25 MPa) is about 1.5 μm for the artifically stiffened experimental setup.

We used a block of Westerly granite (from Westerly, Rhode Island, United States) for the experiments reported in this paper. The granite block was cored and polished to ring specimens. The outer diameter is 53.98 mm and the inner diameter is 44.45 mm. The rock rings were glued into the steel sample grip, and ground flat on a surface grinder to a height of 2.4 mm. The fault surfaces were then hand ground to a uniform roughness using #60 SiC powder on a glass plate. The ring specimens were jacketed both inside and outside by inner split Teflon rings and outer O-rings (Figure S2).

In the rotary shear sample geometry used in this study, the normal stress on the fault surface is a sum of the confining pressure and the axial stress. At the start of an experiment, confining pressure was raised to 20 MPa and servo-controlled within the measurement precision of 0.05 MPa. Axial load was then applied to bring the normal stress to 25 MPa. Axial load was also servo-controlled, generally to within the measurement precision of 0.07 MPa (7).

Shear displacement δ and shear stress τ are calculated from the total rotation R [*] and the torque Γ [Nm] as follows (8):

$$\delta = \frac{4\pi}{3}\frac{R}{360}\frac{r_{out}^3 - r_{in}^3}{r_{out}^2 - r_{in}^2}, \quad [1]$$

$$\Delta\tau = \frac{3}{2}\Gamma\frac{1}{\pi(r_{out}^3 - r_{in}^3)} \quad [2]$$

where r_{out} and r_{in} are outer and inner radii of the sample ring, respectively. Data were collected at a sampling rate of 50 Hz throughout the experiments.

2. Servo control resolution and resulting velocity resolution

Figure S5A shows measured shear stress and resolver displacement and inferred sample slip (from Eq. 5, main text) from a 10,000 s hold which started from steady-state sliding at a velocity of 0.03162 μms^{-1}. During the pre-hold steady state sliding the shear stress is constant, but shows some high-frequency oscillations due to electronic noise. During this time the resolver displacements increase at a constant rate (not shown on the plot due to the sensitive scale of the resolver plot). For the same reason the inferred sample displacements are also not shown during steady sliding. During the hold the resolver (load-point) displacement is servo-controlled to be constant ($V_{\rm lp} = 0$). But, as shown in Figure S5B, the resolver position undergoes abrupt variations having a magnitude of slightly less than 10 nm (these are control system corrections, arising from the finite resolution of the resolver), which is consistent with the expected 9.2 nm resolution for the resolver displacement. The measured shear stress as shown in Figure S5 helps to understand what is occurring in terms of actual fault slip and resolver load-point motion during the hold, even in the time intervals where the resolution of the resolver leads to uncertainty in the load-point motion. During the periods between the 9.2 nm "spikes" when the resolver signal is constant, the shear stress is slowly increasing (Figure S5B). Referring to equation (5) of the main text, this can only be due to forward motion of the load point or backward motion of the fault. Given that backward motion of the fault is impossible without changing the sign of the shear stress, forward motion of the load point must occur that is too small to be measured by the resolver. The reason for this forward drift of the displacement and shear stress between the servo corrections is likely that oil in the hydraulic cylinders slowly leaks past the internal piston in them due to pressure differences in the two chambers that arise from a combination of their different internal areas and the externally applied force. However, continued forward motion of the load eventually results in enough motion that it is measured by the resolver. The servo control using the resolver as feedback then corrects the load-point position, moving it back to the intended constant value. This results in a rapid decrease in the shear stress as is shown in Figure S5B. The calculated fault slip in Figure S5 assumes that during the hold the load point displacement is zero, which is correct at the scale of the hold portion of Figure S5A, and so the gradual overall decay of the shear stress and the gradual overall increase in fault slip shown there is correct. However, on the scale of Figure S5B the incorrect assumption of no

displacement of the load point between the corrective spikes, together with the observed increase in the shear stress, leads to a erroneous calculation of a decrease in fault slip between the spikes. Immediately following each servo correction, the decrease in the shear stress leads to a calculated increase in fault slip.

As the indicated slope on the plot of fault slip in Figure S5A shows, the slip velocity near the end of this specific hold gets as low as 0.02 nms^{-1}. The largest error in estimating the slip rate must accompany near instantaneous variations in the resolver position by 9.2 nm. Across such rapid resolver motions, the sample's motion at an average at 0.02 nms^{-1} can be ignored. This resolver motion would, under these circumstances, lead to a change in the shear stress of magnitude $\Delta\tau = k\sigma\delta_{1p}$. To estimate the magnitude of slip rate variations this change in shear stress could cause, which is the uncertainty in our slip rate estimation, we turn to the rate-state friction equations, which seem to do a good job describing our experiments at the lowest sliding speeds we can resolve. Assuming the load point motion to be nearly instantaneous, one can assume that this shear stress change will be balanced by the change in friction due almost entirely to the direct velocity effect. This assumption is likely accurate even for 'non-instantaneous', sub 9.2 nm, excursions in the resolver. From eq. 1 of the main text, we get

$$V = V_0 \exp\left(\frac{\Delta\tau}{a\sigma}\right) = V_0 \exp\left(\frac{k\sigma\delta_{1p}}{a\sigma}\right). \quad [3]$$

Using $k = 0.065\,\mu m^{-1}$, $\delta_{1p} = 9.2\,\text{nm}$ and $a = 0.013$, we get $V/V_0 \sim 1.05$ for positive changes in load point displacement suggesting that the actual velocity does not vary by more than 5% from the average of 0.02 nms^{-1}. Note that this estimate is independent of the long-term, background slip rate as long as the ~ 10 nm fluctuations in load-point displacement occur at orders-of-magnitude faster rates than the slip rate. Therefore, the velocity resolution in these experiments is roughly 5% near the termination of long holds.

3. Notes on the Slip and Aging equation fits to the velocity steps

The methodology used to fit the velocity step decrease data shown in the main text is described under the *Materials and Methods* section accompanying the main text. Here we present a brief discussion on the principal features of these fits. The data from the velocity step decreases shown in Figure 1 in the main text were fit with the Slip equation in two ways – a common fit to a subset of the velocity steps and independent fits to all the velocity steps. For the first of these, the initial $3\mu m$ of post-step friction evolution for one each of 1.0, 2.0, 2.5, 3.0 and 3.5 order steps were fit with a common set of Slip equation parameters. These Slip equation fits are shown in Figures S7A-E. Even though the fits to the steps are reasonable, the post-peak friction evolution is underestimated for the 3.0 and 3.5 order steps (Figure S7A and B) but overestimated for the 1 order step (Figure S7E). In particular, these patterns of misfit seem consistent with too small a value of D_c being used for the fits compared to the data from the two largest step which, at the same time, is slightly too large compared to the data from the smallest step. The value of a for these fits is around 0.013 and $D_c \sim 2\mu$m. Figures S7F-J show the slip rate evolution predicted by the corresponding fits to the friction data. All the fits capture the slip rate excursions reasonably well. It is also noteworthy that the value of $a - b$ derived from the fits is -0.0031 which is in good agreement with the independent estimate of $a - b$ in Figure S6. The Slip equation simulations in Figures 1, 2 and 3 and Table 1 in the main text use the parameters derived from these first set of fits.

To further explore the slight step-size or slip-rate dependence of D_c suggested by the fits in Figure S7, we tried a second family of Slip equation fits to the velocity steps by allowing independent fits to every velocity step decrease in Figure 1 with $a - b = -0.003$. As with the fits in Figures S7 and S8, we fit friction evolution over only the first 3 μm of post-step slip. Figure S9 shows these fits while Figure S10 the corresponding predictions of slip rate. While the data from each individual step is very well matched by the particular parameter choices for that fit, the Slip equation parameters do vary somewhat across these different fits. The most pronounced is the variation of D_c, but even that varies by a factor of less than two. These variations can be seen in the posteriors of both a and D_c in Figures S11A-D. The panels A and B in these figures show the posteriors for the 0.5 and 1.0 order steps alone, while the panels C and D show their corresponding variations for the MCMC fits to the larger steps. Comparing the posteriors of a between Figures S11A and C immediately reveal that there is no statistically significant variation in a between the different models required to fit the vastly different step sizes. Interestingly, the variations in D_c required to fit the various 0.5 order steps was also found to be similar to the variations in D_c required to fit the larger steps. When either the value corresponding to the minimum RMSE fit or the median value of D_c are extracted from these posteriors and plotted as a function of the post-step velocity (inset of Figure S11B), the observed variations in D_c turn out to be within the bootstrapped 95% confidence levels suggested by the posteriors inferred from the MCMC fits. Therefore, given the data variations between the different velocity steps of the same step size, it is difficult to conclude that the variations in D_c observed between the fits to the different sized steps necessarily reflect a trend with step size.

With the Aging equation, we have tried only the one-fit-to-all-steps strategy for the velocity step decreases in Figure S7A-E. These fits are shown in Figure S8A-E. As is to be expected from the arguments presented in the main text, the Aging equation generally does a worse job of fitting the post-minimum friction evolution than the Slip equation with no a priori constraints on $a - b$ (red curves in Figure S8A-E). With the root mean square misfit for all the velocity steps weighted equally, the joint best fit to all of the steps did the best job of fitting the medium-sized steps. In particular, for the largest slip rate decreases the fitted friction evolved to steady state over a smaller slip scale than the data. Also, these fits required $a - b = 0.0035$ which is clearly at odds with our independent estimate of $a - b = -0.003$ in Figure S6. Bhattacharya et al. (6) have shown that the Aging equation needs to be velocity strengthening in order to match the monotonically decreasing stress relaxation trajectories observed during long holds. In keeping with the view that holds are similar to the pre-minimum strength evolution

following large velocity steps (Figure 3C-F in the main text), it seems reasonable that only velocity-strengthening Aging equation solutions allow the friction minima to monotonically decrease in response to increasing step size at a rate comparable to the data. For completeness, we also present Aging equation fits to the data with the a priori constraint $a - b = -0.003$ (purple curves in Figure S8A-E). In keeping with the analytical prediction that a velocity-weakening Aging equation fit would predict much shallower friction minima compared to the data for large velocity steps (as discussed in the main text), these fits grossly under-predict the friction minima for the largest velocity steps. This shows that the failure of the Aging equation to fit the velocity step decrease data is inherently connected to its failures in fitting stress evolution during long holds (6). The Aging equation simulations in Figures 1, 2 and 3 and Table 1 in the main text use the parameters derived from these set of fits with the Aging equation.

4. Slip scale for friction evolution following large Aging-equation velocity-step decreases

One of the features of Aging equation simulations incompatible with the 'short slip distance' strengthening observed after the stress minimum in our velocity step decreases is the ever-decreasing length scale of strength evolution with increasing step size (Figure 1B in the main text). Here, we rationalize this feature for velocity decreases that push the interface far below steady state ($V\theta/D_c \ll 1$). To do this, we approximate the post-minimum friction evolution under the Aging formulation as

$$\frac{d\mu}{d\delta} \approx b\frac{d}{d\delta}\ln(\theta) \approx \frac{b}{D_c}\frac{D_c}{V\theta}, \qquad [4]$$

where δ is slip distance. The first equality in Eq. (4) follows from equation (1) with a near-constant sliding velocity (equal to V_f), and the second from the Aging law approximation $\dot{\theta} \approx 1$ far below steady state. In Figure S12, we show that for Aging-equation velocity step decreases, $V\theta/D_c$ shortly beyond the strength minimum (we choose an arbitrary level at 0.9 of the total stress drop) is only modestly larger than the velocity ratio V_f/V_i. This is because V is slightly above V_f and θ is modestly above $\theta_i = D_c/V_i$. Thus, the Aging formulation predicts that the rate of restrengthening $d\mu/d\delta$ just beyond the stress minimum increases almost as rapidly as V_i/V_f.

The above result is for a finite-stiffness system. For an instantaneous velocity step applied directly to a surface previously sliding at steady state, or equivalently a load-point velocity step in an idealized infinite-stiffness system, the Aging equation (2a) in the main text can be integrated analytically for θ and the result substituted into the friction equation (1). Relative to the future steady-state value, the friction is (9)

$$\Delta\mu = b\ln\left(1 + \frac{(V_f - V_i)e^{-\delta/D_c}}{V_i}\right) . \qquad [5]$$

Differentiating with respect to δ and evaluating at the stress minimum ($\delta = 0$),

$$\frac{d\mu}{d\delta} = \frac{b}{D_c}\left(\frac{V_i}{V_f} - 1\right). \qquad [6]$$

For large step decreases $V_i/V_f \gg 1$, $d\mu/d\delta$ increases linearly with V_i/V_f. The Tullis rotary shear apparatus is stiff enough that Aging formulation simulations that use its stiffness qualitatively capture this infinite stiffness result.

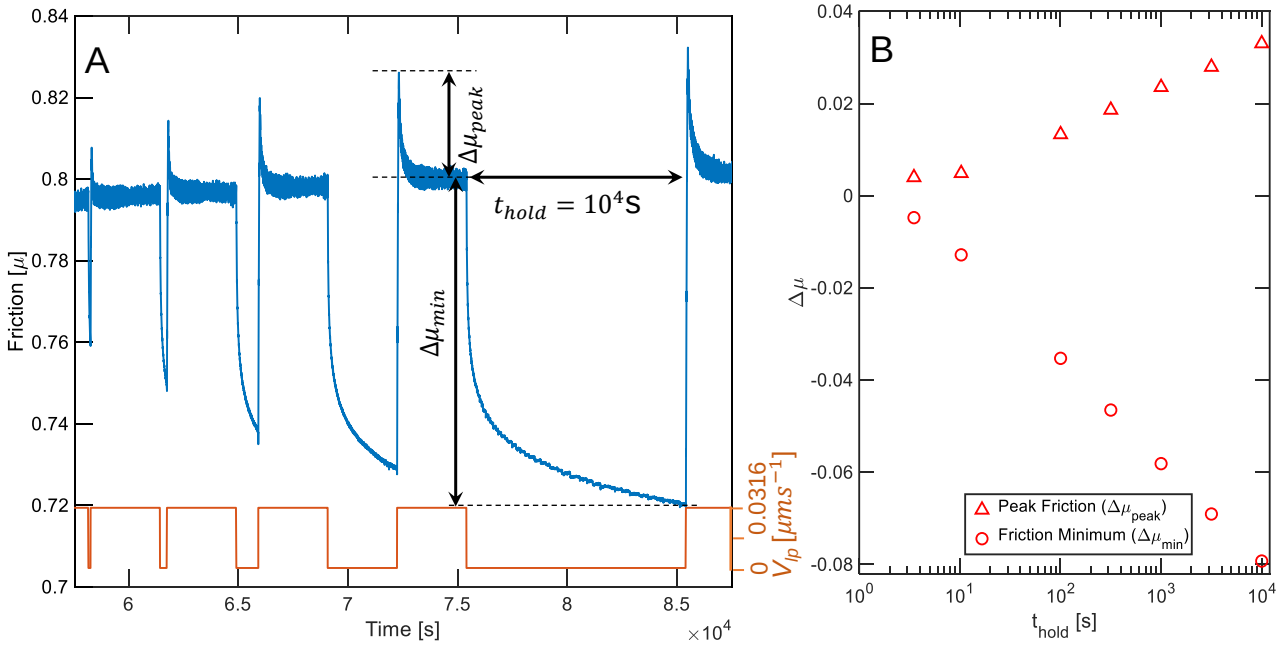

Fig. S1. Frictional strengthening in laboratory slide-hold-reslide experiments. (A) Variation in friction (blue) and loading rate (orange) with time during a sequence of slide-hold-reslides for the section of the experiments shown in Figures 4B and E. (B) Evolution of peak friction and the friction at the end of the holds with hold duration from the same experiment section. The data shows the classical linear with log hold duration increase in the peak friction. Also note the also nearly linear with log hold duration decrease in the minimum friction shown by the data. Such continual decrease in the friction minimum is generally inconsistent with a velocity weakening Aging RSF model (6).

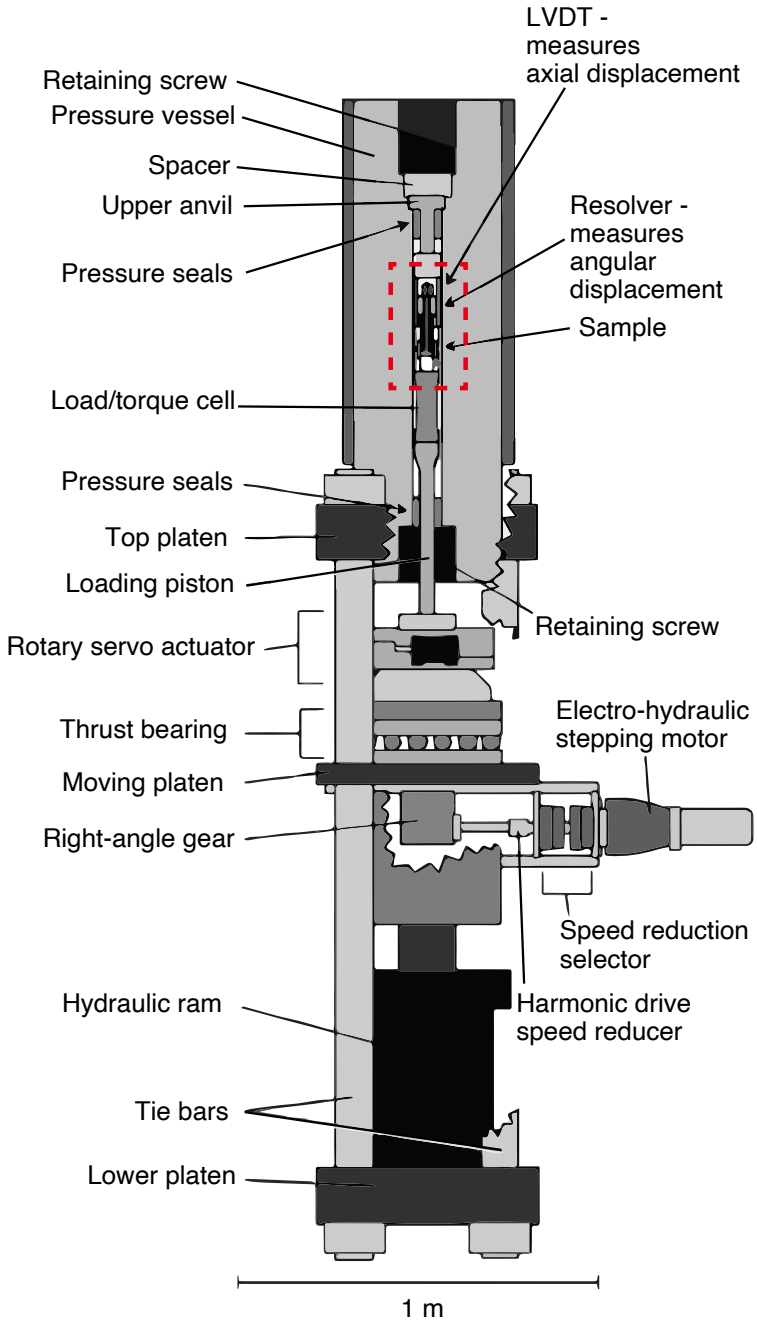

Fig. S2. Schematic of the rotary shear apparatus at Brown used for the experiments in the paper. The major parts are labeled.

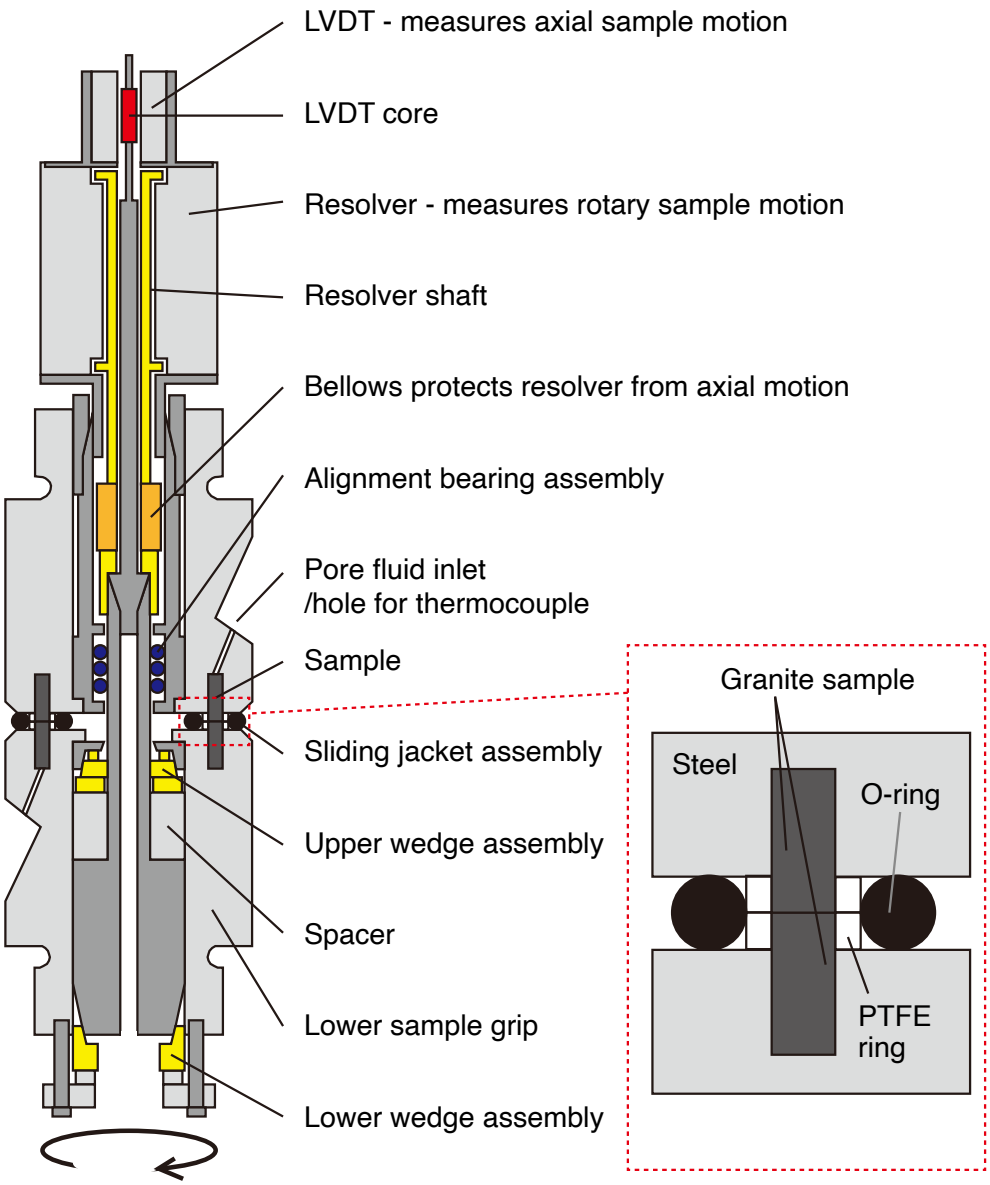

Fig. S3. Close-up view of the region enclosed by the dashed, red rectangle in Figure S2 showing the pressure vessel, sample assembly and the measurement set-up. On the right inset, the sample assembly showing the granite ring sample, the sample grips and the O-ring.

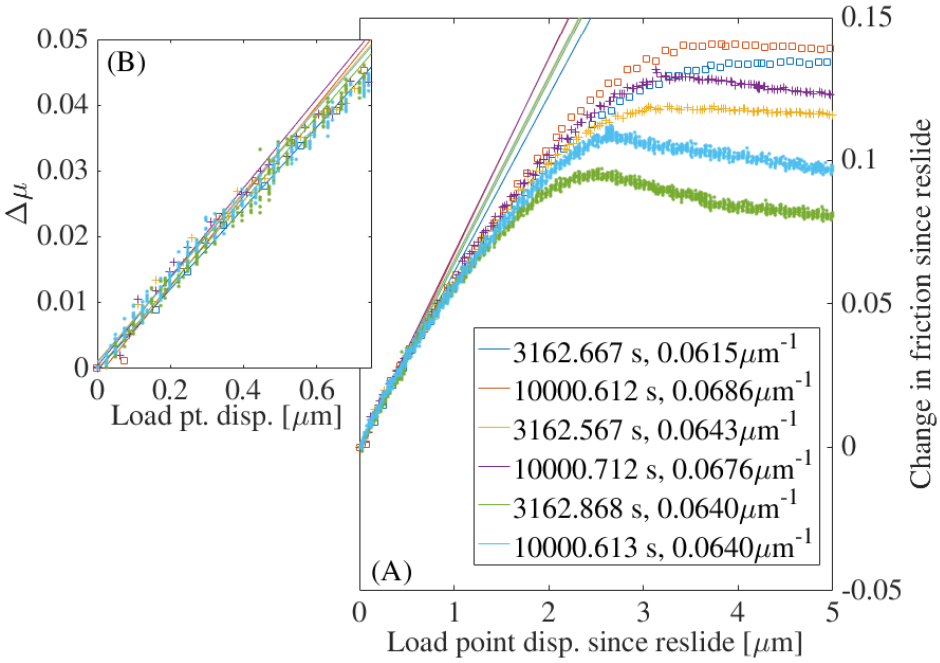

Fig. S4. Estimation of stiffness for the servo-controlled, artificially stiffened, rotary shear apparatus. (A) Change in friction ($\Delta\mu$) since reslide versus load point displacement (δ_{lp}), both evaluated since the start of the reslide, following holds of ~ 3000s and ~ 10000s at three reslide rates each – squares at 1 $\mu\mathrm{ms}^{-1}$, crosses at 0.3162 $\mu\mathrm{ms}^{-1}$ and dots at 0.03162 $\mu\mathrm{ms}^{-1}$. The initial reloading rate fixes the stiffness; we used 1/7th of the total number of points between the onset of reslide and eventual peak strength for the fits. (B) A zoomed in version of the fits in (A). We use a stiffness of 0.065 $\mu\mathrm{m}^{-1}$ in our analyses.

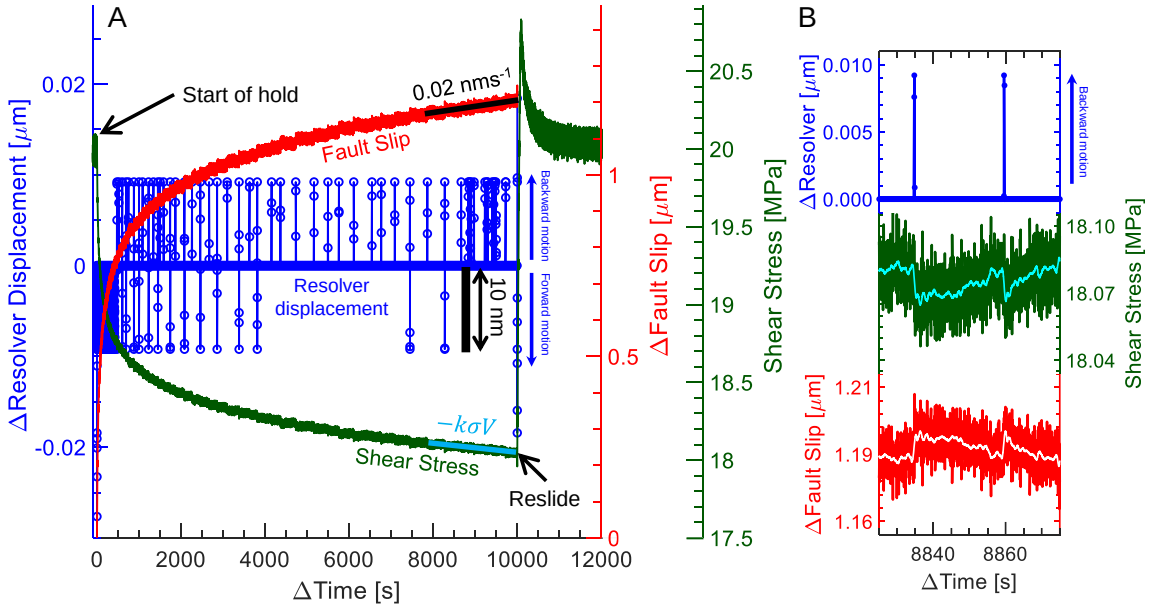

Fig. S5. (A) Shear stress, load-point displacement, and fault slip during a 10,000 s hold, following steady-state sliding at 0.0316 $\mu\mathrm{ms}^{-1}$. The load-point displacement is servo-controlled to be constant during the hold to a resolution of 10 nm, which allows attaining very small fault-slip displacements and velocities. The shear stress (green curve) is measured with a torque-cell and the load-point displacement (blue curve) is measured with a high-resolution resolver, both being mounted internal to the pressure vessel. Note that some blue data points from the resolver appear to suggest even better resolution than 10 nm, but these data points result from some temporal averaging; they reflect contributions from values at the nominal one as well as from values differing by 10 nm. Averaged over time windows encompassing many resolver "corrections", small changes in shear stress result from relaxation of the frictional stress due to slowing fault slip. This fault slip can be calculated (red curve) using the known stiffness of the rock between the fault and the load-point and knowledge of the load-point displacement. As shown by the slope of the red curve near the end of the hold, the average fault slip velocity becomes as low as 0.02 nms^{-1}. The corresponding rate of decrease in shear stress, $k\sigma V$ with $V = 0.02\mathrm{nms}^{-1}$, is also shown to capture the trend in the shear stress data very closely. As discussed in the text, the variations in this average velocity are estimated to be only 5 percent due to the 10 nm displacement corrections at the load-point resulting from the servo control resolution. (B) Zoomed in view of the transient shear stress changes in response to the resolved fluctuations in the resolver position between 8825 and 8875 seconds. Note how rapid stress decreases always accompany resolvable backward movements of the load point. Also note the subsequent slower increase in shear stress even when the load point shows no resolvable motion. This can only happen when the resolver moves forward by less than 9.2 microns even though the data shows it to be nominally at rest.

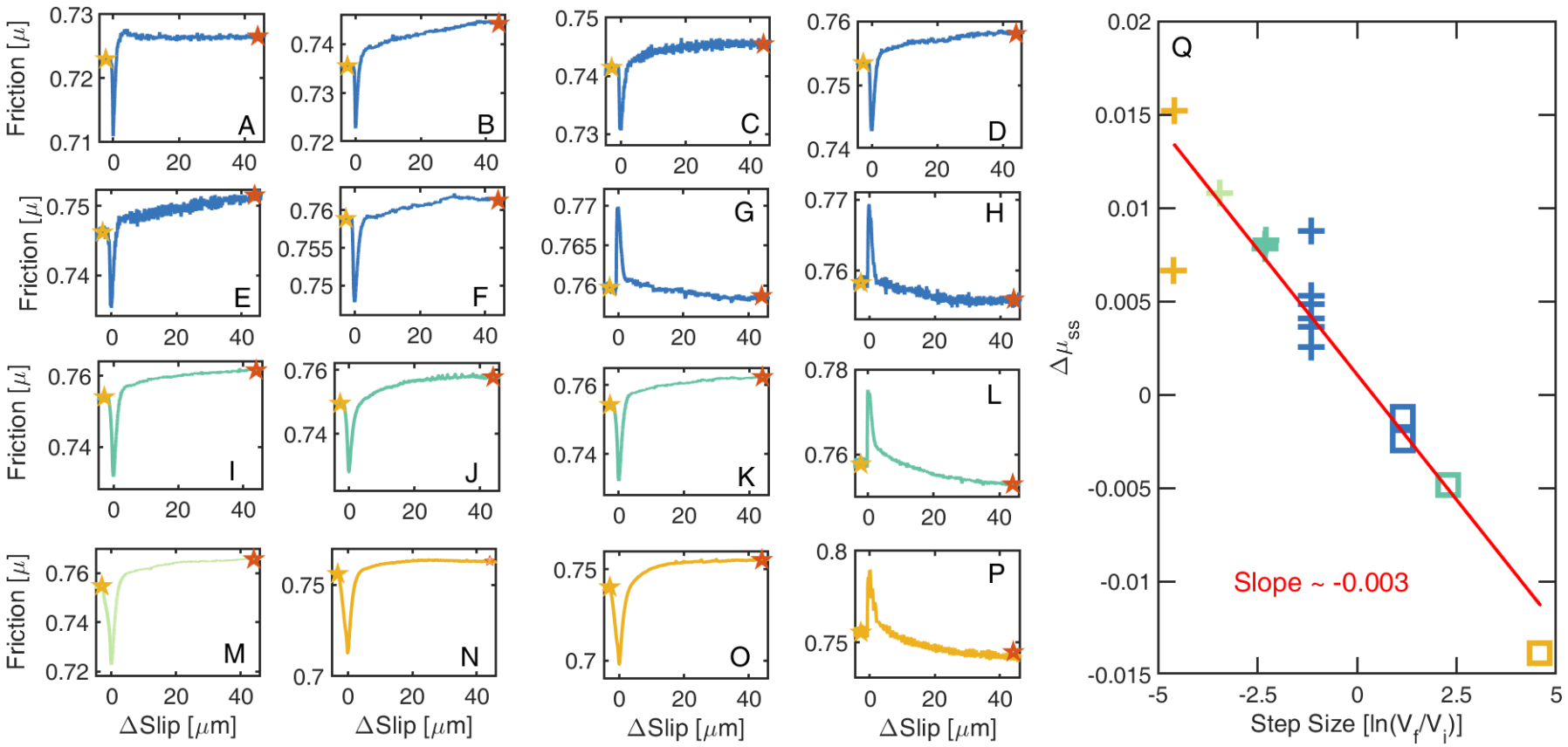

Fig. S6. Estimation of $a - b$ from all the 0.5 to 2.0 order velocity steps in Figure 1. (A)-(P) Velocity step increases and decreases of 0.5 to 2.0 orders showing steady state velocity weakening beyond total accumulated slip of 120 mm (16 in total) since the beginning of the experimental run. Color coding of the data according to step sizes is identical to the one used in the figures in the main text. The steady state change in friction, $\Delta\mu_{ss}$, is measured between the points shown by yellow and red stars in each panel. In particular, the post-step steady state is assumed at 40 μm of slip since the onset of the step to avoid long-term transients in the data. For most of the larger velocity steps excluded from this analysis, measurements had either not been continued for long enough to reach steady state or the shear stress did not saturate to a steady state level consistent with the vast majority of other velocity steps. (Q) $\Delta\mu_{\rm ss}$ versus $\ln(V_{\rm f}/V_{\rm i})$ from the sequence of velocity steps shown in (A)-(P). Mean $a - b \sim -0.003$ explains the data well.

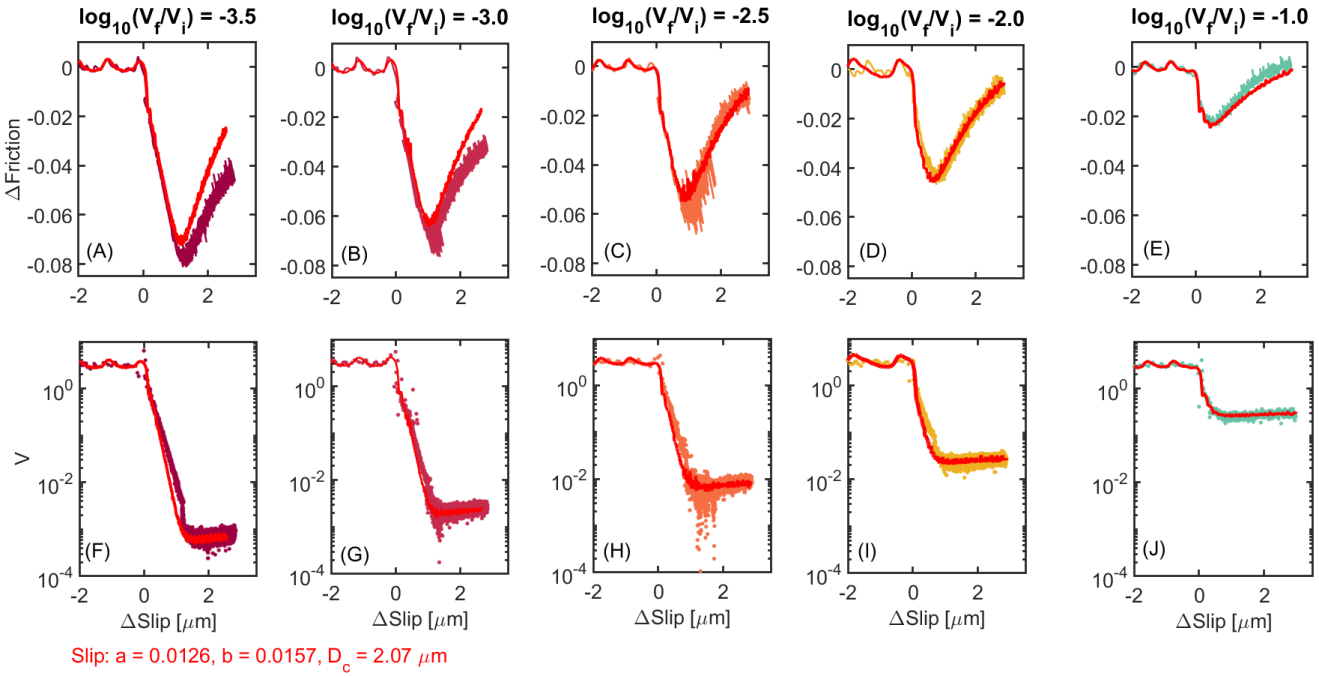

Fig. S7. Fits to a subset of the sequence of large velocity step decreases from Fig. 1A with the Slip equation jointly with the same set of parameters. Friction evolution was modeled for only the first 3 μm of slip following the onset of the velocity step to avoid potential problems with the long-term stress transients seen in some of the steps. (A)-(E) Fits to the stress data, (F)-(J) predictions of slip rate from the corresponding fits to the stress data. The data is color coded identically to the figures in the main text, Slip equation fits are shown in red. Note that $a - b$ was not pre-constrained; the inversion constrained a value which agrees well with our independent, a priori estimate of $a - b$.

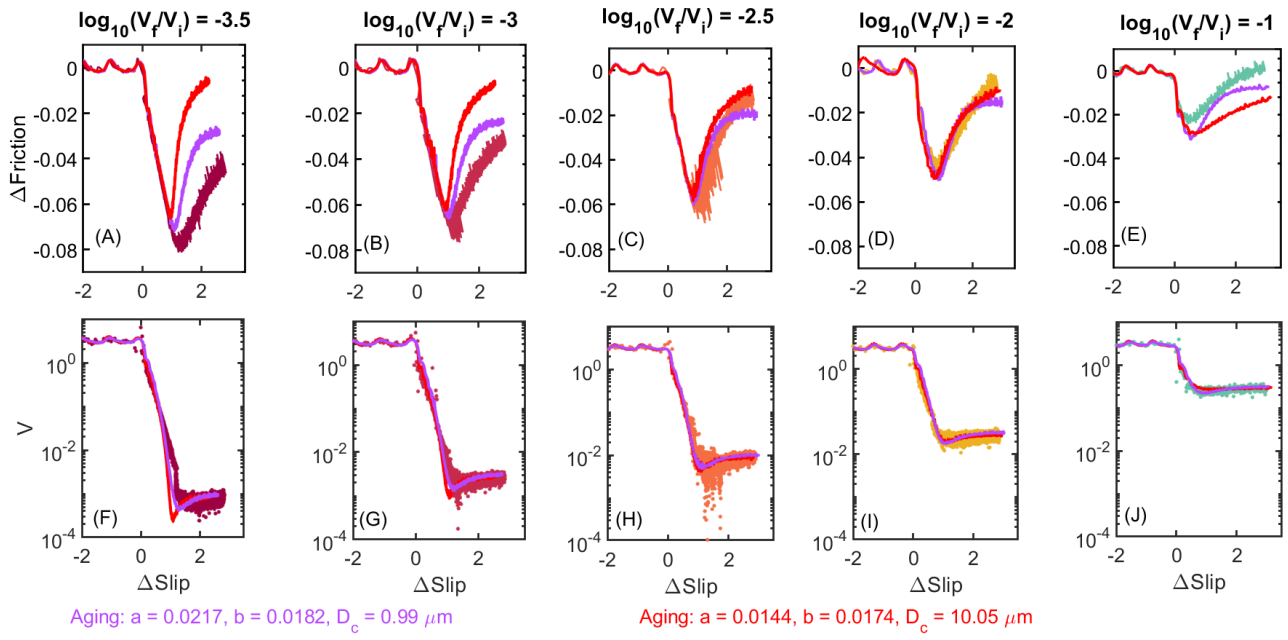

Fig. S8. Aging equation fits, with equivalent weights, to the same sequence of velocity steps in Fig. S7. (A)-(E) Fits to the stress data, (F)-(J) predictions of slip rate from the corresponding fits to the stress data. The data are once again color coded identically to the figures in the main text and Figure S7. The Aging equation fits in red were constrained with $a - b = -0.003$. Aging equation fits with $a - b$ unconstrained are shown in purple. Note that the fits with $a - b$ unconstrained naturally require $a > b$, unlike the corresponding Slip equation fits.

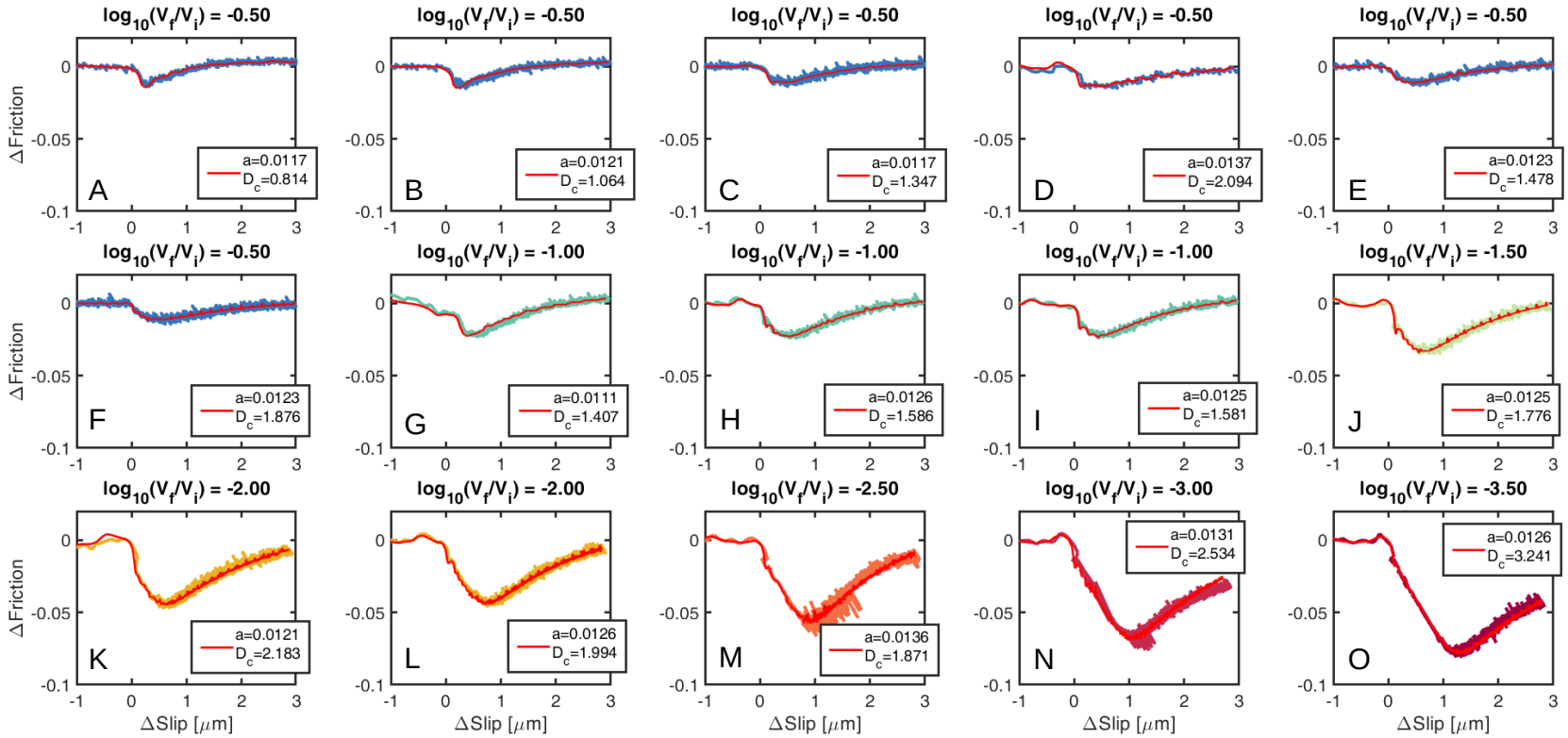

Fig. S9. Independent Slip equation fits to each of the velocity step decreases in Figure 1 from the main text. The different parameters for each of these fits are shown in the legend in each panel. Each of these fits was constrained with $a - b = -0.003$. The data are color coded according to step size identically to Figures 1, 2 and 3 in the main text. The red curves show the modeled friction response.

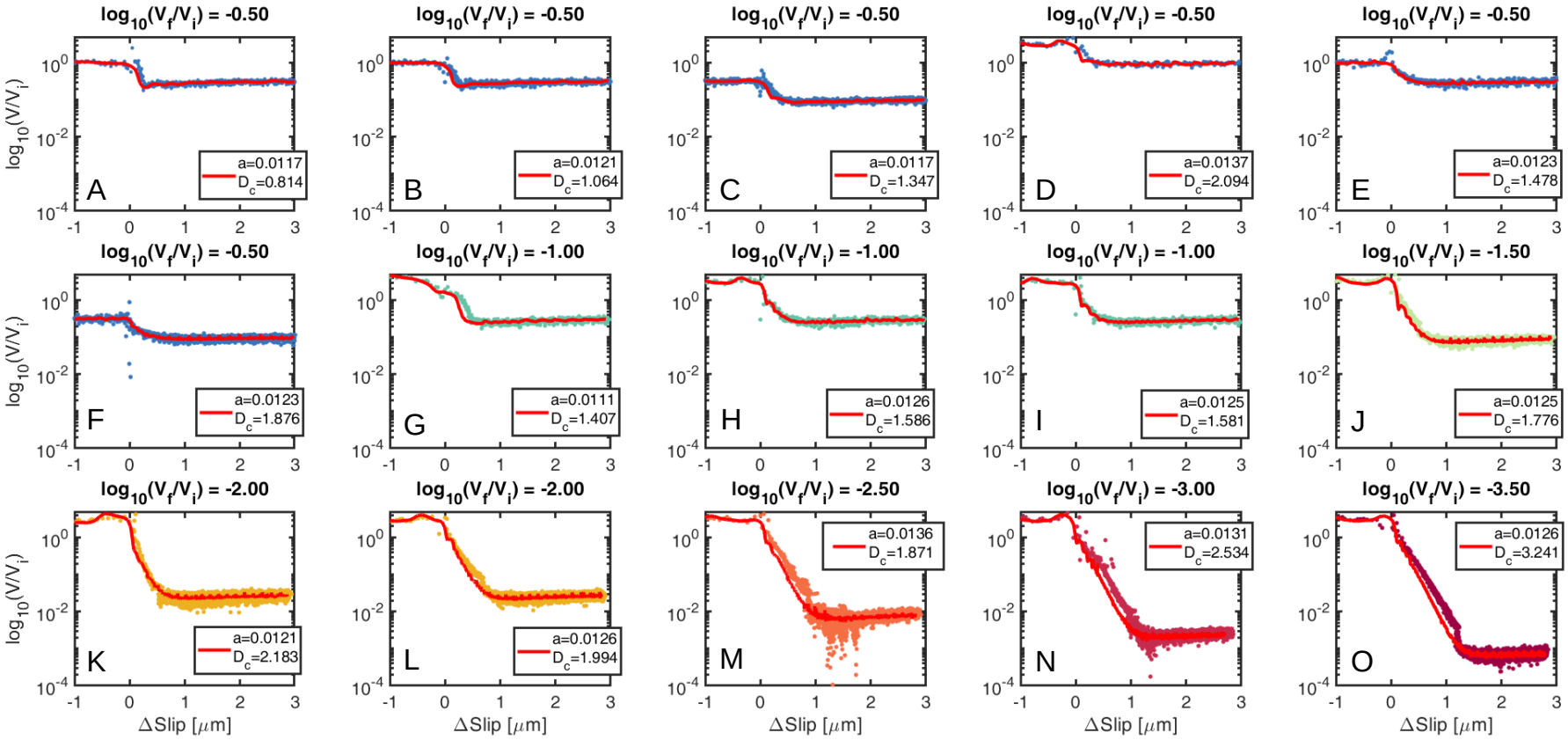

Fig. S10. Velocity predictions from the Slip equation fits in Figure S9 compared to estimated velocity variations from the data. Once again, the data are color coded according to step size identically to Figures S9. Red curves show slip rate variations estimated from the modeled fits in Figure S9.

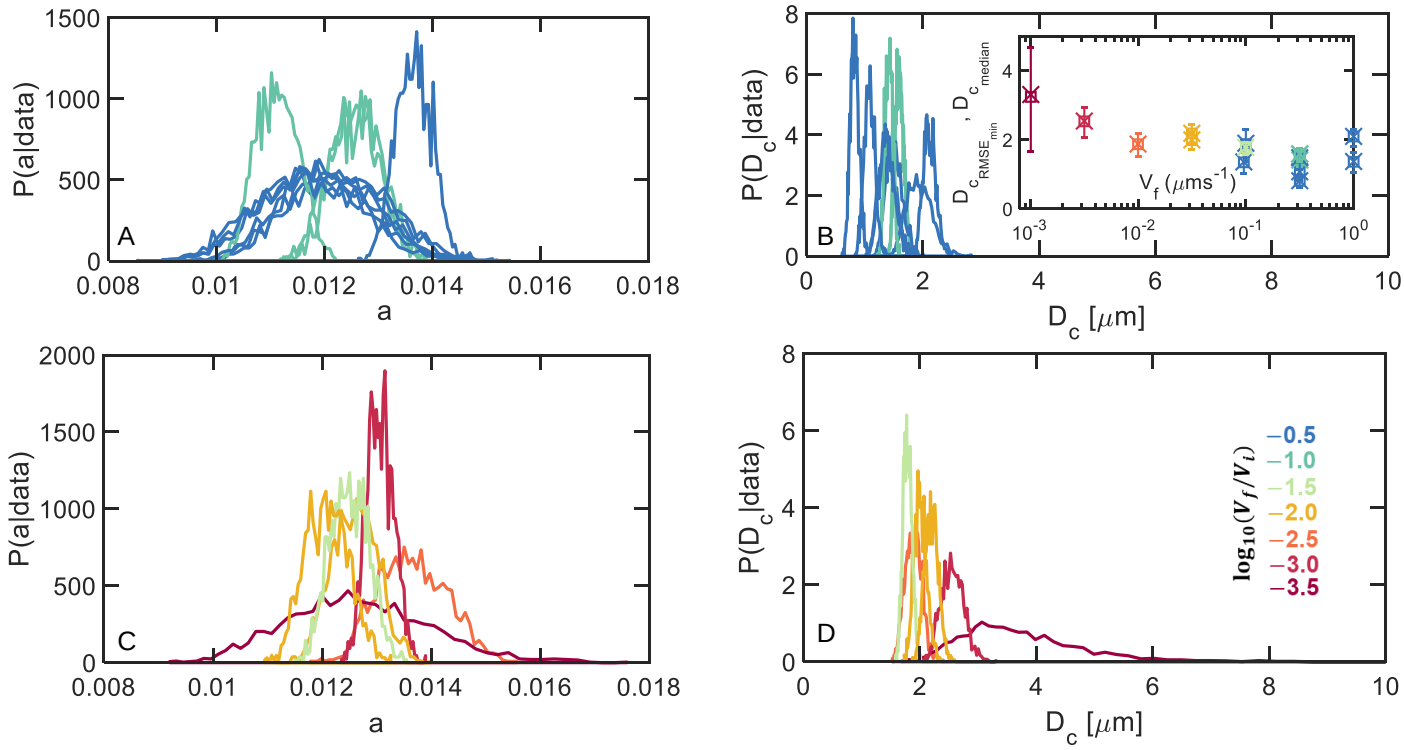

Fig. S11. Posteriors for a and D_c from the Slip law fits in Figure S9. (A) and (B) show the posteriors for 0.5 and 1 order steps, (C) and (D) for the larger step decreases. The posteriors are color coded according to step size identically to Figures 1, 2 and 3 in the main text. Inset of (B) - D_c estimates from the minimum RMSE error parameter combination found from sampling the posterior (squares) and the medians from the posteriors (crosses with 95% error bars).

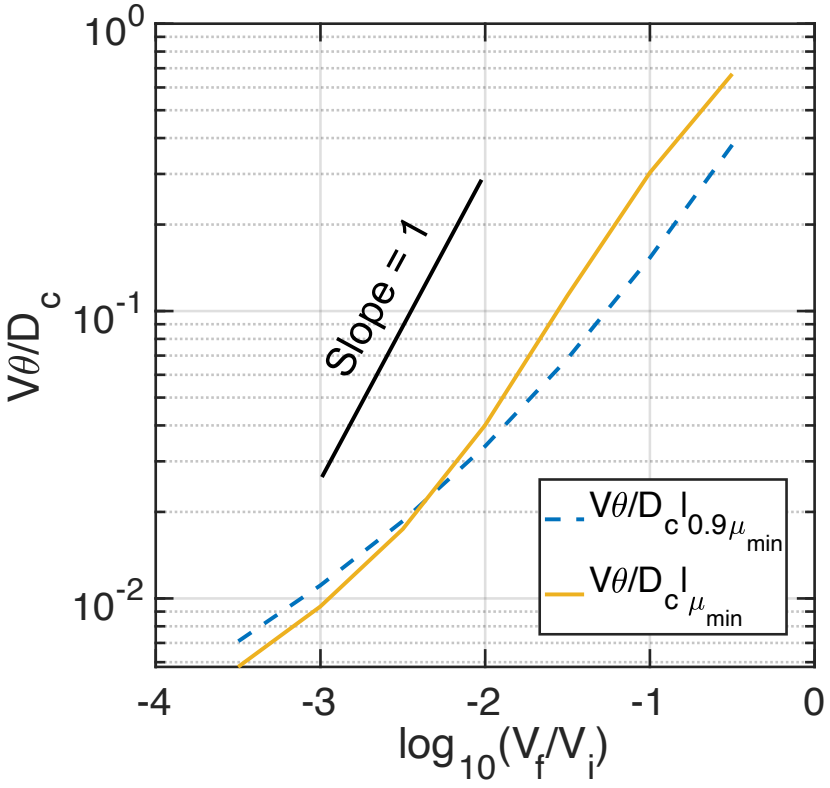

Fig. S12. Evolution of the value of $V\theta/D_c$ evaluated at strength minimum $\mu_{\min}$ (yellow solid line) and at $0.9\mu_{\min}$ post-minimum (blue dashed line) with size of velocity step decreases for the Aging equation. Model parameters were derived by fitting the velocity-step decreases in Figure S8 with the Aging equation (Table 1). Note that $V\theta/D_c$ at $\mu_{\min}$ (and also at $0.9\mu_{\min}$ post-minimum) decreases sub-linearly with increasing step size.

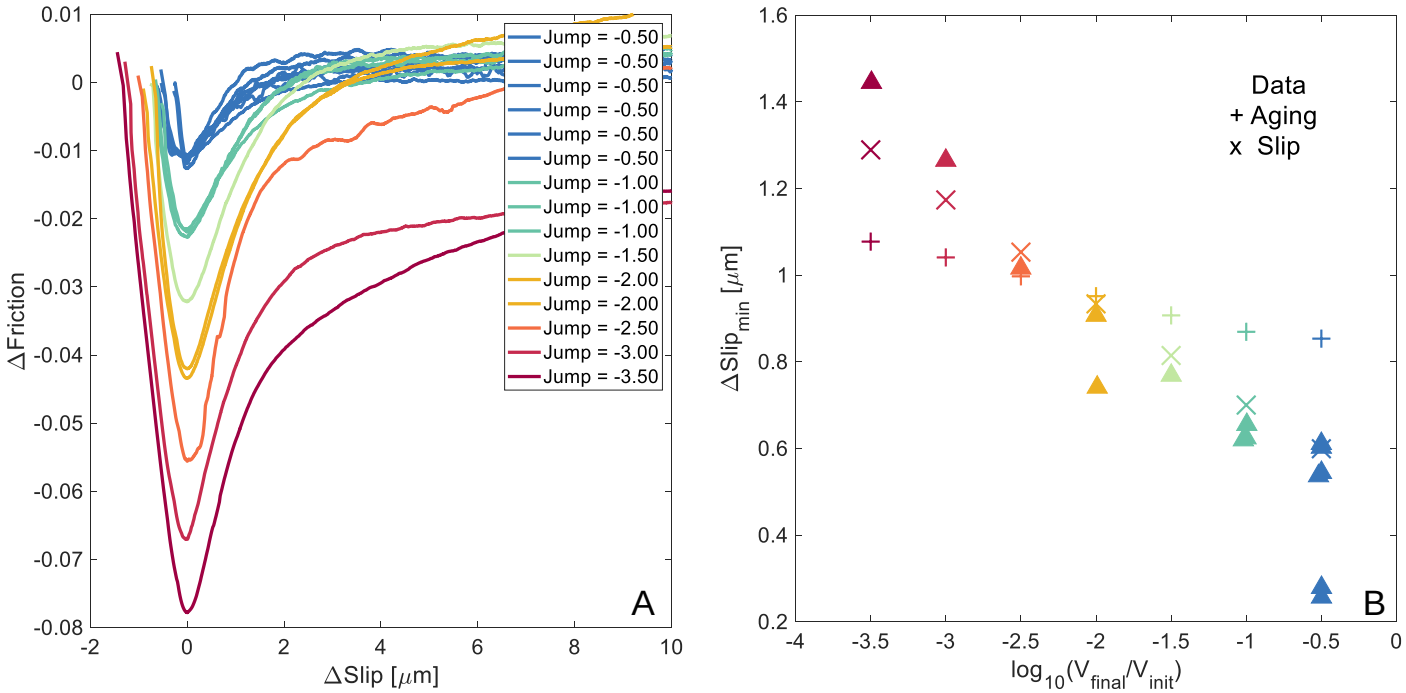

Fig. S13. Estimation of the slip accrued between the onset of the velocity step decreases in Figure 2A and the stress-minima – (A) The velocity-step data is shown again for comparison; (B) Comparison between the pre-minimum slip distance from the data (triangles), Aging equation simulations from Figure 3A (+ signs) and Slip equation simulations from Figure 3B (x signs). The color of the symbol correspond to the color coding of velocity-step size in A. Note how only the Slip equation simulations agree well with the data. The Aging equation simulations also show a quasi-linear increase in the pre-minimum slip accumulation with log step size but its rate of increase is several times smaller than that of the data.

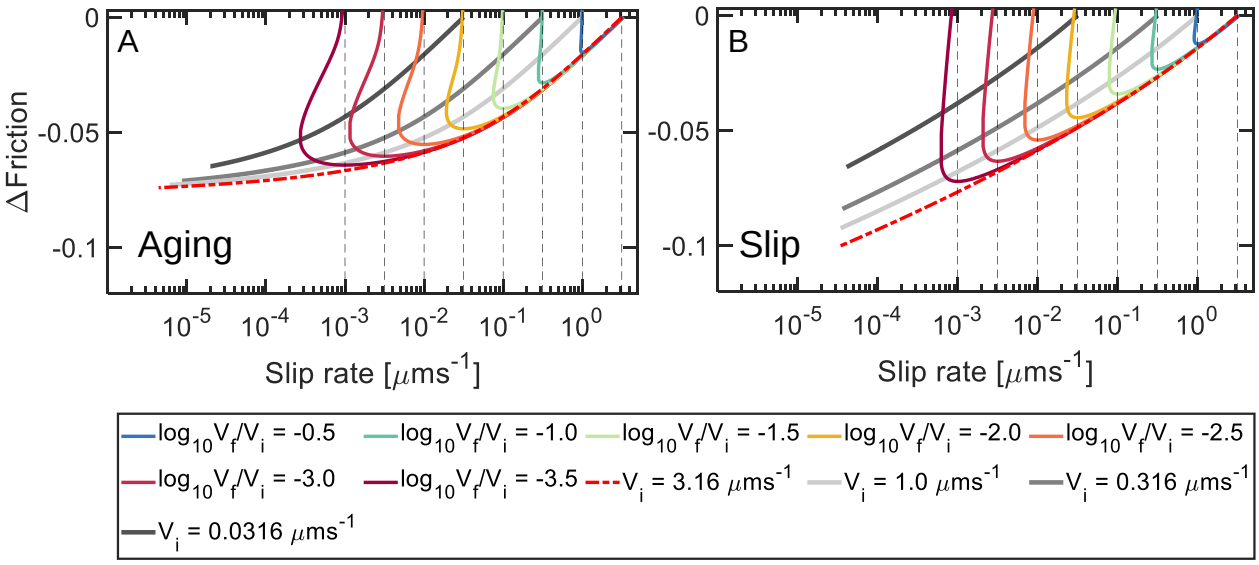

Fig. S14. Comparison of slip rate evolution during the different steps and 3163s long holds from the same set of numerical simulations shown in Figures 3(A) and (B) in the main text with the same color code. As in Figures 3(A) and (B), here (A) shows Aging and (B) Slip equation simulations. Note that the minimum velocity attained during Slip equation holds is nearly independent of the pre-hold slip rate. For the Aging equation, holds of equal duration attain smaller minimum slip rates if the initial slip rate is higher.

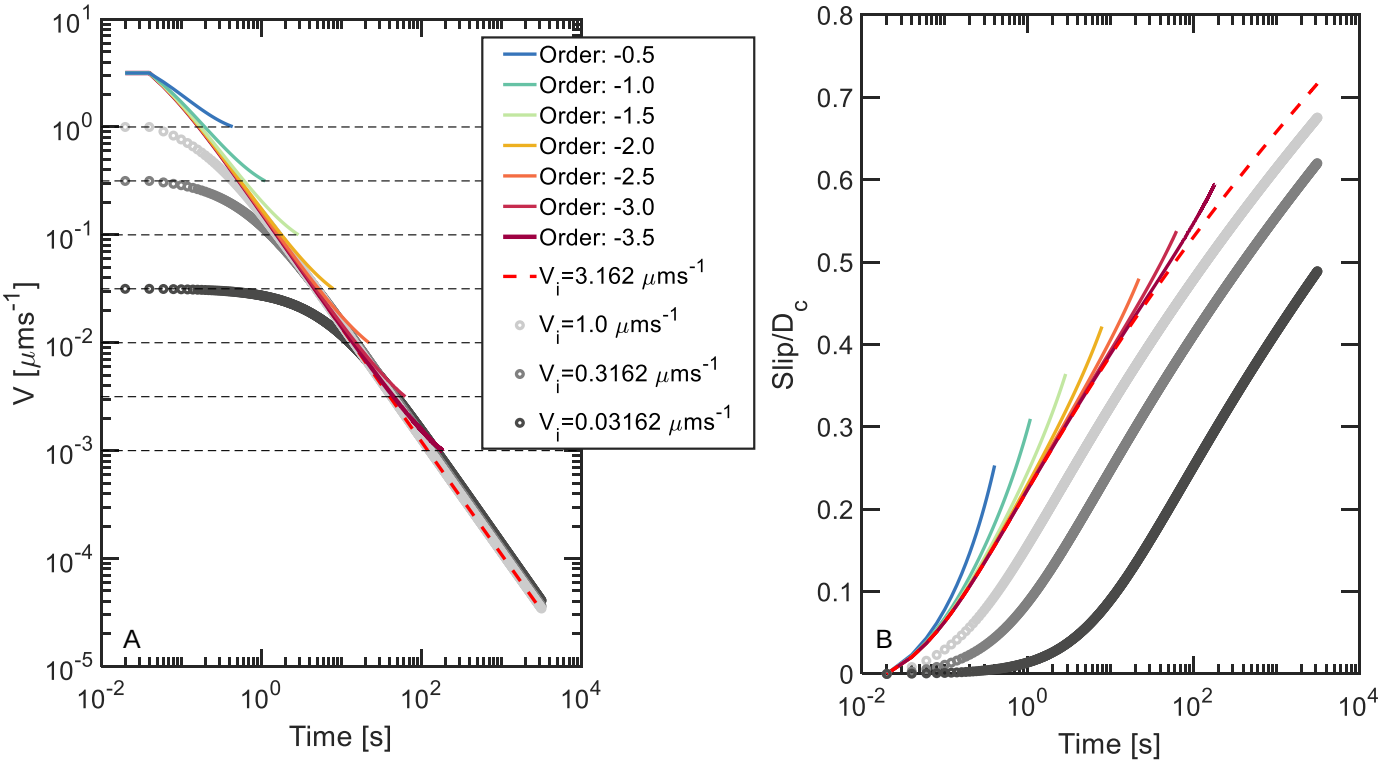

Fig. S15. Simulations of velocity steps and holds with the Slip equation parameters derived from fits to the velocity step data from Figure S7 (Table 1 in the main text). (A) Variation in slip rate with time during the pre-minimum friction evolution for the velocity steps and holds shown in Figure 3C. Note that the largest velocity steps in the experimental suite of our study access the same slip rates as hold durations of several 100s of seconds. The color scheme is identical to Figure 3. (B) Normalized slip accumulated with time for the same set of simulations as in (A). Note that the different pre-hold slip rates lead to different amounts of slip during the hold.

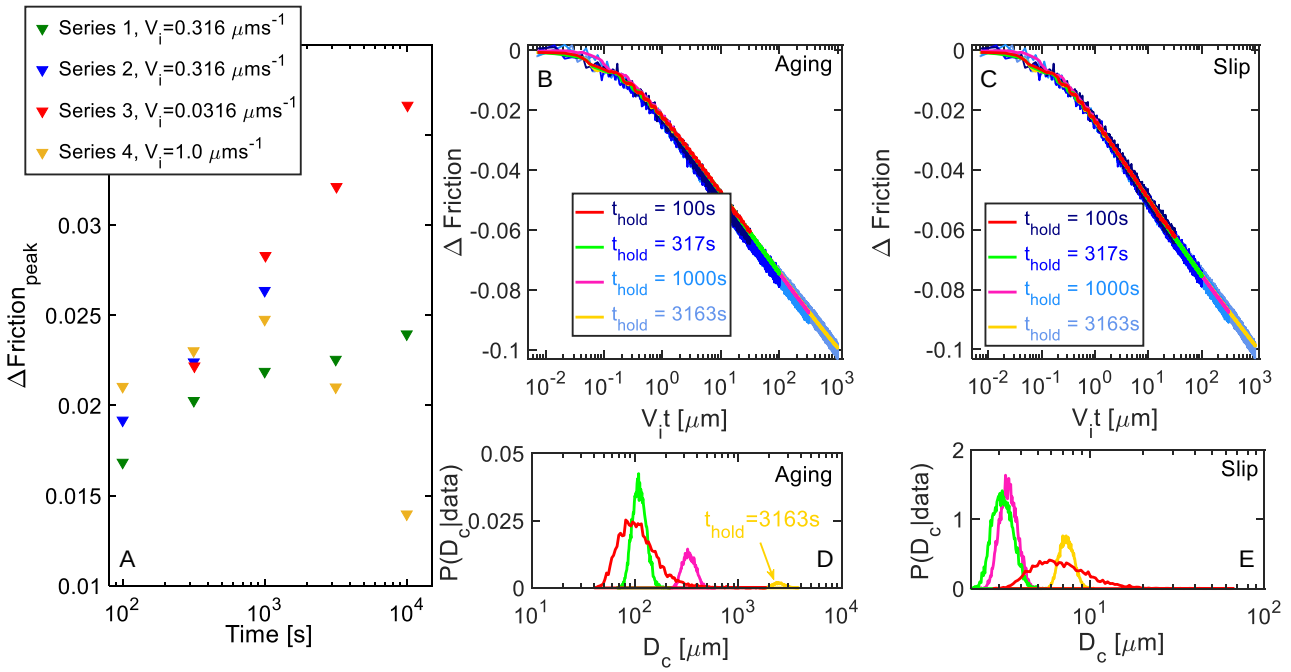

Fig. S16. (A) Peak strength evolution with hold time for all the sets of slide-hold-slides run during our experimental suite. Note the anomalous decrease in peak strength for hold durations longer than 1000 s for the set of holds with $V_i = 1\mu\text{ms}^{-1}$. This is an additional reason we chose not to fit the two longest holds at $V_i = 1\mu\text{ms}^{-1}$. (B) Aging equation joint fits to 100s – 3163s-long holds with $V_i = 0.316\mu\text{ms}^{-1}$ (Series 1 in A, not included in the main text). The 10000s hold is not included due to the MCMC not converging for this hold duration. Note that Series 2 in A is used in Figures 4A and D in the main text as representative data for $V_i = 0.316\mu\text{ms}^{-1}$. We made this choice since those data closely reproduced the hold-duration dependence of peak strength for the other sets of holds at different V_i. (C) Same as (B) but for the Slip equation. The inferred parameters from these joint fits are listed in Table 1. (D) and (E) show posteriors for D_c when the holds in panels (B) and (C) are fit individually with a different a and D_c inferred from each hold, with $a - b = -0.003$ fixed. Note that the trend of inferring larger D_c for longer hold durations with the Aging law is seen here as well, though obscured slightly by the anomalous posterior for the 100s hold with both the Aging and Slip equations.

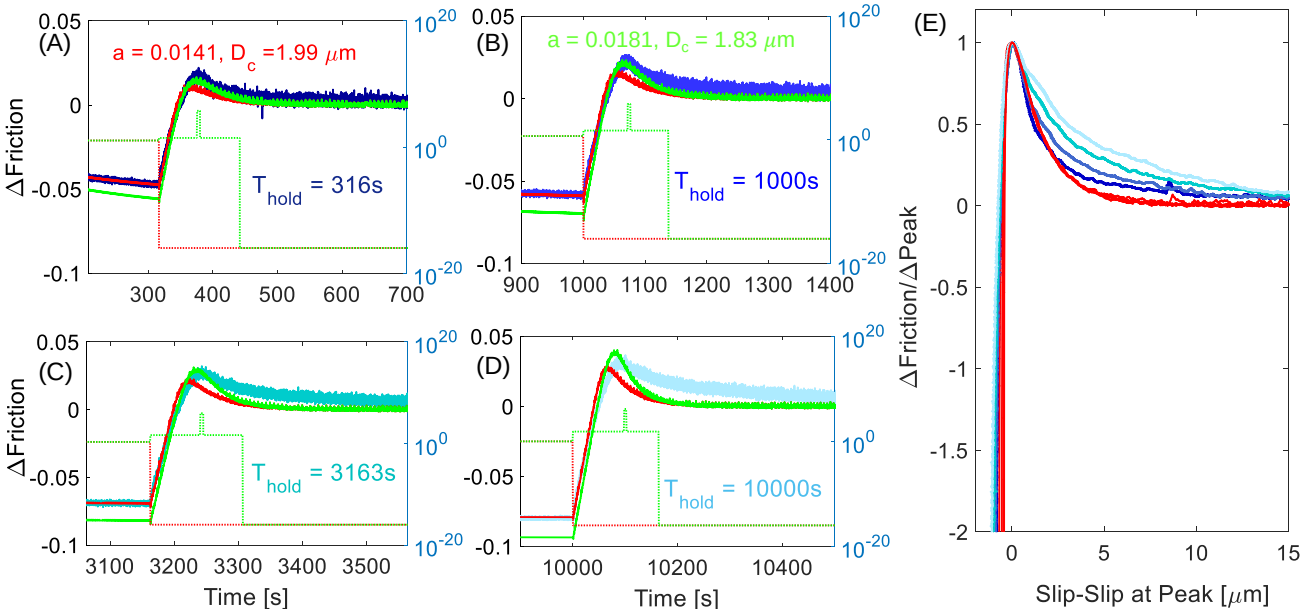

Fig. S17. Slip equation fits and predictions of the static friction peaks and evolution length scales following reslides for the set of holds in Figure 4E. (A)-(D) show the reslides following holds of duration 316 sec - 10000 sec with longer holds plotted respectively in progressively lighter shades of blue. Zero friction level is fixed at the pre-hold steady-state value of the friction coefficient. The red curves in each panel are the predictions of the fits to the holds alone taken from Figures 4E, the corresponding weights used are depicted as red dotted lines (weighting scales indicated on right axis). The green curves in each panel show fits which have been weighted equally between the hold and a fixed time window covering the reslide from its beginning to future steady state (green dotted lines). Differential weighting is applied around the peak friction to achieve maximum fidelity to the observed peak strength. Note how, when compared to the fits to the holds alone, the green curves underestimate the shear strength at the end of the preceding holds. (E) shows the strength evolution following the reslides in (A)-(D) but normalized by the peak to residual strength drop measured at 15 μm of post-peak slip. Also shown are the corresponding predictions of the fits to the holds alone scaled identically to the data (red curves). The darker to lighter shades of blue correspond to increasing hold durations as in (A)-(D). The slip weakening length scale appears to increase with hold duration.

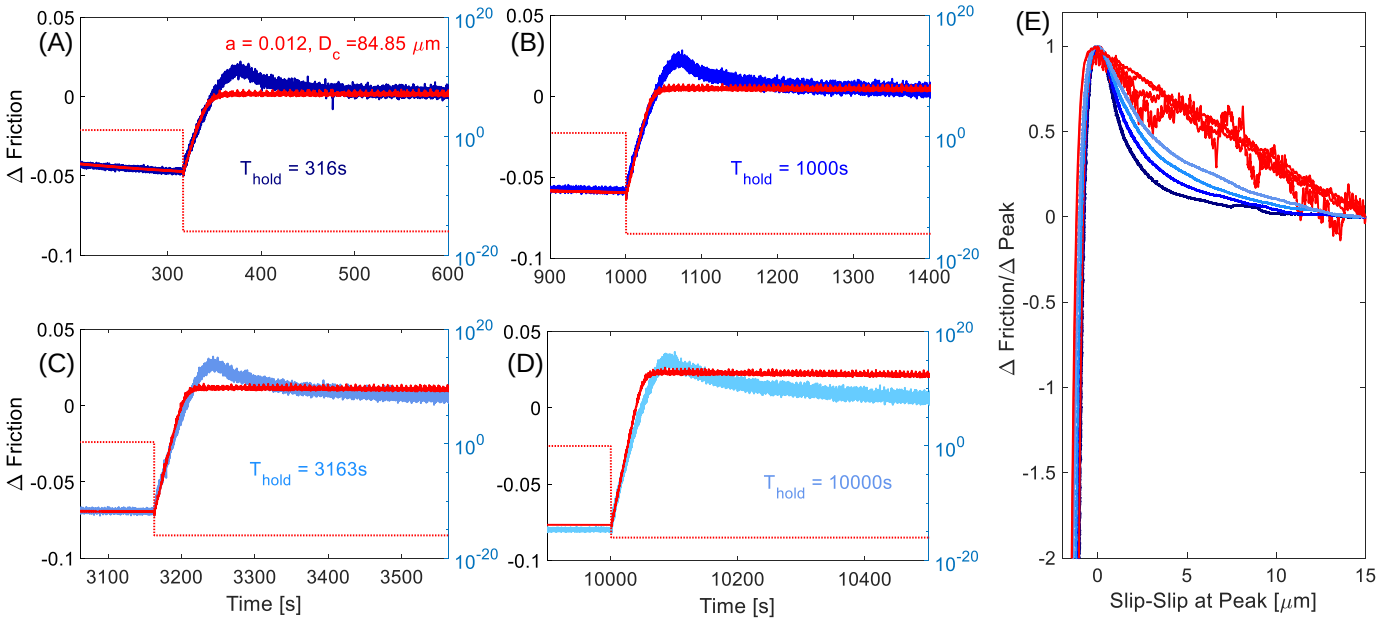

Fig. S18. Aging equation predictions of the static friction peaks and evolution length scales following reslides for the set of holds in Figure 4E. (A)-(D) show the reslides following holds of duration 316 sec - 10000 sec with longer holds plotted respectively in progressively lighter shades of blue. Zero friction level is fixed at the pre-hold steady-state value of the friction coefficient. The red curves in each panel are the predictions of the fits to the holds alone taken from Figures 4E, the corresponding weights used are depicted as red dotted lines (weighting scales indicated on right axis). (E) shows the strength evolution following the reslides in (A)-(D) but normalized by the peak to residual strength drop measured at 15 μm of post-peak slip. Also shown are the corresponding predictions of the fits to the holds alone scaled identically to the data (red curves). The darker to lighter shades of blue correspond to increasing hold durations as in (A)-(D). The Aging equation predicts strictly linear slip-weakening post-peak friction similar to its prediction for large velocity steps.

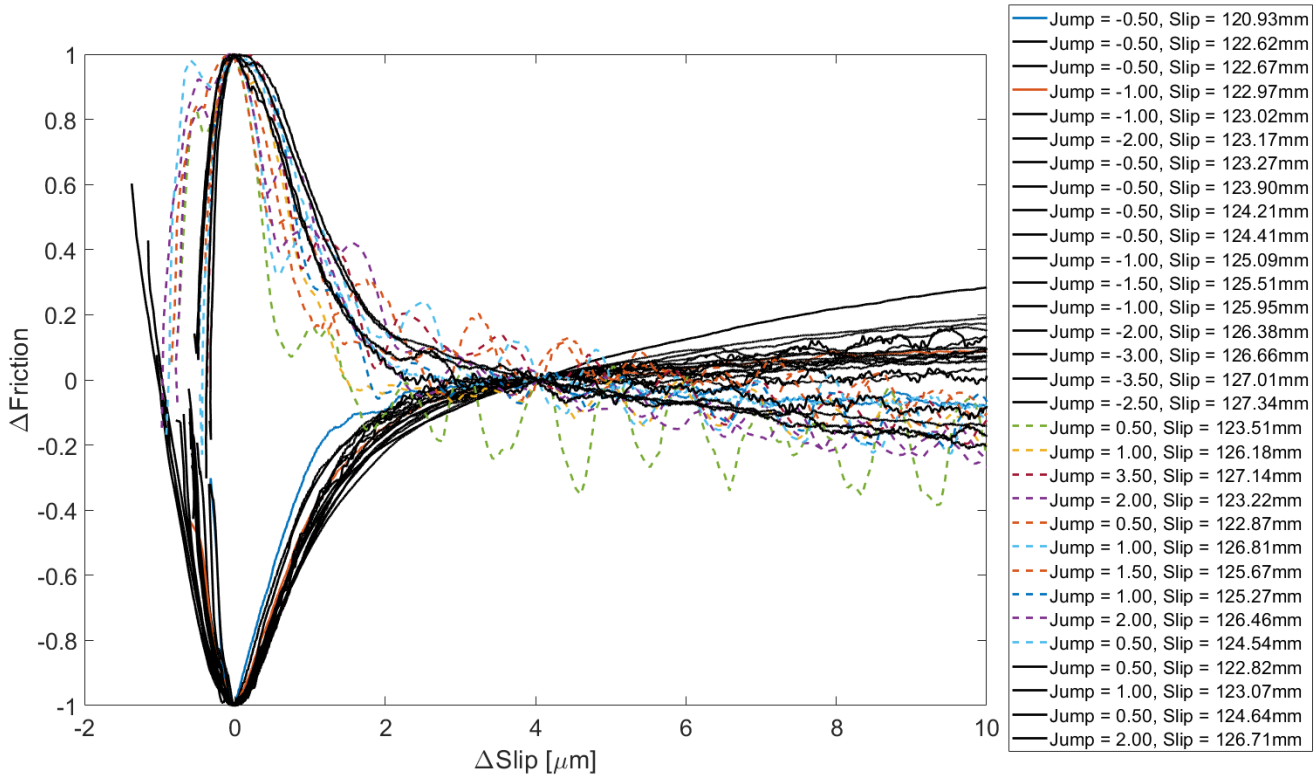

Fig. S19. All the velocity steps in the experimental run from which the ones reported in Figure 1A were chosen. As in Figure 1A, the changes in friction are measured from its value at $4\mu\mathrm{m}$ and are normalized by the maximum amplitude of this change. All the velocity steps shown in Figure 1A are shown in black. Most of the step increases were difficult to control, owing to the velocity-weakening nature of the sliding surface.

References

1. Weeks JD, Tullis TE (1985) Frictional sliding of dolomite: A variation in constitutive behavior. *Journal of Geophysical Research: Solid Earth* 90(B9):7821–7826.
2. Tullis TE, Weeks JD (1986) Constitutive behavior and stability of frictional sliding of granite. *Pure Appl. Geophys.* 124(3):383–414.
3. Beeler NM, Tullis TE, Blanpied ML, Weeks JD (1996) Frictional behavior of large displacement experimental faults. *J. Geophys. Res.: Solid Earth* 101(B4):8697–8715.
4. Tullis TE (1997) Friction measurement apparatus in *Instruments of Science: An Historical Encyclopedia*, eds. Bud RF, Warner DJ. (Garland, New York), pp. 249–251.
5. Beeler N, Tullis TE, Weeks JD (1994) The roles of time and displacement in the evolution effect in rock friction. *Geophys. Res. Lett.* 21:1987–1990.
6. Bhattacharya P, Rubin AM, Beeler NM (2017) Does fault strengthening in laboratory rock friction experiments really depend primarily upon time and not slip? *J. Geophys. Res.: Solid Earth* 122(8):6389–6430. 2017JB013936.
7. Beeler NM, Tullis TE (1997) The roles of time and displacement in velocity-dependent volumetric strain of fault zones. *J. Geophys. Res.: Solid Earth* 102(B10):22595–22609.
8. Tsutsumi A, Shimamoto T (1997) High-velocity frictional properties of gabbro. *Geophysical Research Letters* 24(6):699–702.
9. Ampuero JP, Rubin AM (2008) Earthquake nucleation on rate and state faults – aging and slip laws. *J. Geophys. Res.* 113:B01302.